Supplementary Information for

Contributions of biological and physical dynamics to deglacial CO_2 release from the polar Southern Ocean

Yuhao Dai[1,2] * and Jimin Yu[3,1,4]*

[1]Research School of Earth Sciences, Australian National University, Canberra, ACT, Australia
[2]ARC Australian Centre for Excellence in Antarctic Science, Australian National University, Canberra, ACT, Australia
[3]Laoshan Laboratory, Qingdao, China
[4]SKLLQG, Institute of Earth Environment, Chinese Academy of Sciences, Xi'an, China.
*Corresponding authors: yuhao.dai@anu.edu.au, jiminyuanu@gmail.com

Contents of this file

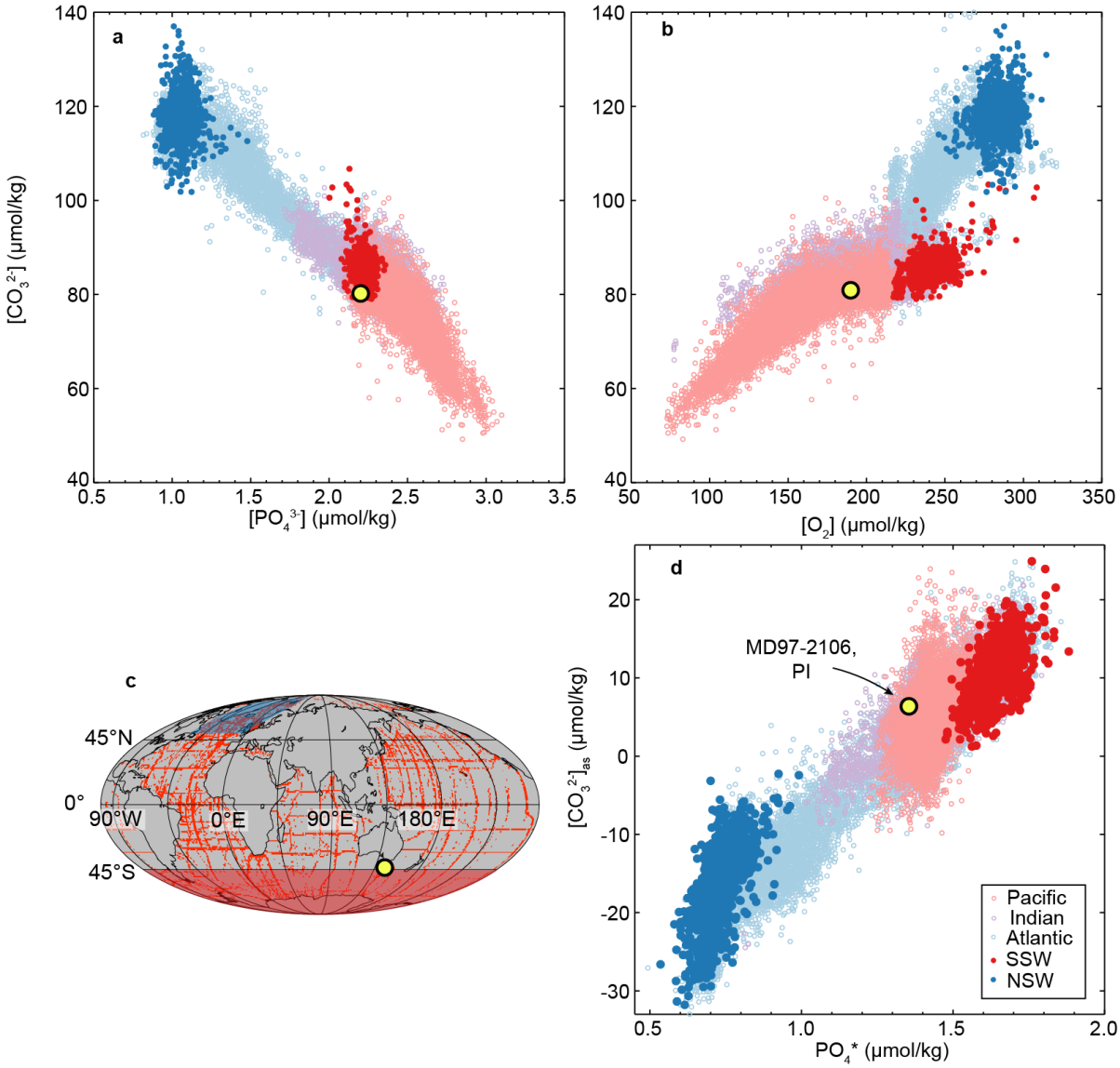

Supplementary Fig. 1. Preindustrial deep ocean biogeochemistry. a, $[PO_4^{3-}]$ versus $[CO_3^{2-}]$, **b,** $[O_2]$ versus $[CO_3^{2-}]$, **c**, Map showing hydrographic locations, **d,** PO_4^* versus $[CO_3^{2-}]_{as}$. Data are from GLODAPv2[1,2]. Data in the Pacific, Indian, and Atlantic oceans are from >2500 m water depths. The Northern Sourced Water (NSW) and Southern Sourced Water (SSW) are defined following Ref. [3]. The yellow circles in **a, b,** and **d** show the preindustrial deep-water biogeochemistry at site MD97-2106. The yellow circle in **c** indicates the location of Site MD97-2106. Red and blue shading regions in **c** highlight regions where SSWs and NSWs, respectively, are defined.

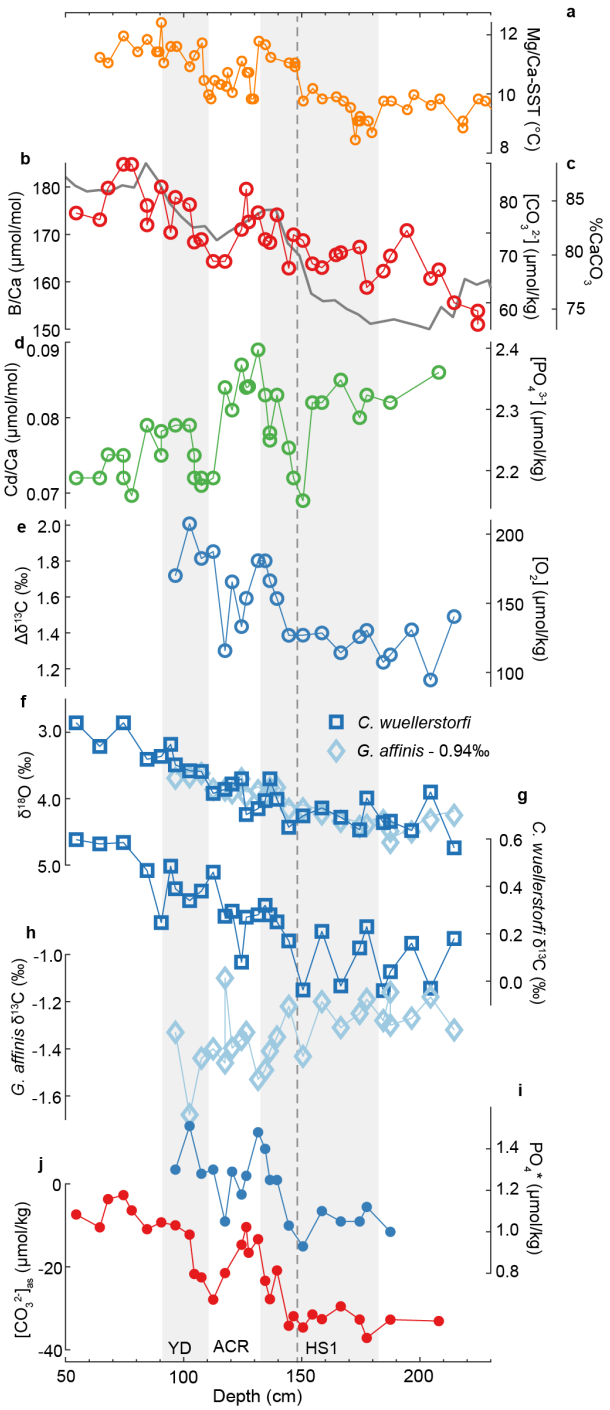

Supplementary Fig. 2. Proxy data against core depth at MD97-2106. a, Sea surface temperature (SST) estimated from Mg/Ca in *G. bulloides*[4]. **b,** *C. wuellerstorfi* B/Ca and the estimated $[CO_3^{2-}]$. **c,** Sedimentary carbonate content (grey curve)[5]. **d,** *H. elegans* Cd/Ca and the estimated $[PO_4^{3-}]$. **e,** $\delta^{13}C$ gradient between *C. wuellerstorfi* and *G. affinis* and estimated $[O_2]$. **f,** $\delta^{18}O$ in *C. wuellerstorfi* (dark blue) and *G. affinis* (light blue), where $\delta^{18}O$ in *G. affinis* is subtracted by 0.94‰ to account for the interspecies offset. **g,** *C. wuellerstorfi* $\delta^{13}C$. **h,** *G. affinis* $\delta^{13}C$. **i,** PO_4^*. **j,** $[CO_3^{2-}]_{as}$. In **b** and **d**, replicated measurements of subsamples are shown as different data points. Grey vertical bars indicate the depth ranges corresponding to the Younger Dryas (YD) and Heinrich Stadial 1 (HS1). Between these two periods is the Antarctic Cold Reversal (ACR). The vertical dashed line shows the depth corresponding to the boundary between early and late HS1.

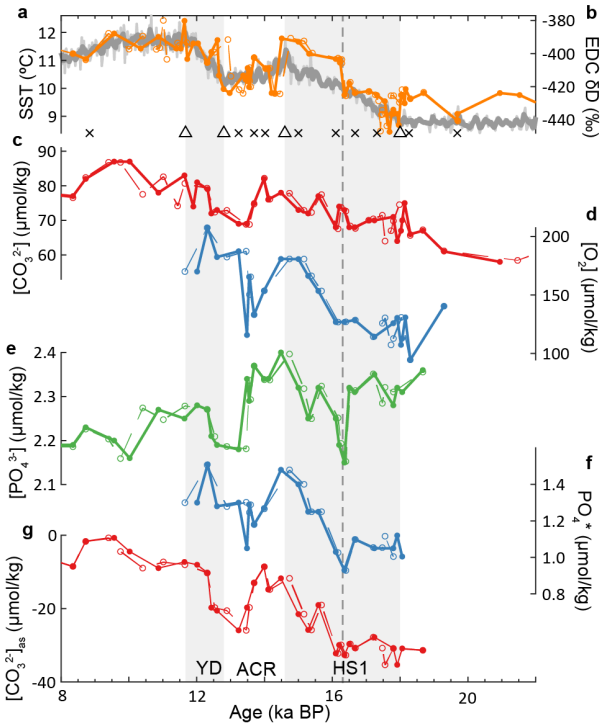

Supplementary Fig. 3. Influences of age control points on records at site MD97-2106. a, Sea surface temperature (SST)[4]. **b,** EPICA Dome C (EDC) δD, a proxy for Antarctic temperature)[6]. Triangles at the bottom are age tie points for SST at site MD97-2106 and EDC δD, and crosses represent ^{14}C dates[4,7]. **c,** $[CO_3^{2-}]$; **d,** $[O_2]$; **e,** $[PO_4^{3-}]$; **f,** PO_4*; **g,** $[CO_3^{2-}]_{as}$. In **a**, **c-g**, solid curves with solid dots are the same as shown in the main text. **a**, **c-g**, dashed curves with empty dots are records based on an alternative age model relying only on radiocarbon dates.

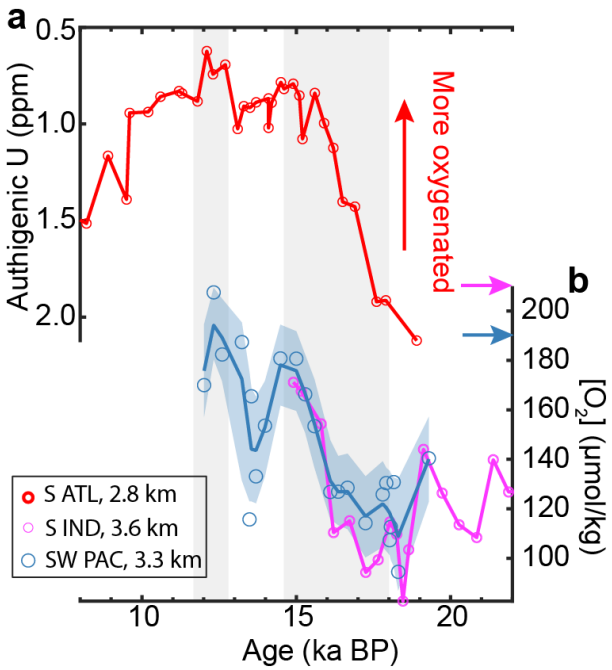

Supplementary Fig. 4. Comparison of deep-water [O_2] at site MD97-2106 to other deep Southern Ocean oxygenation reconstructions. a, South Atlantic Ocean oxygenation based on authigenic uranium[8] (red circles). **b,** South Indian Ocean oxygenation[9] based on benthic carbon isotope gradients (magenta circles), compared to [O_2] at site MD97-2106 (blue circles with error envelope; this study).

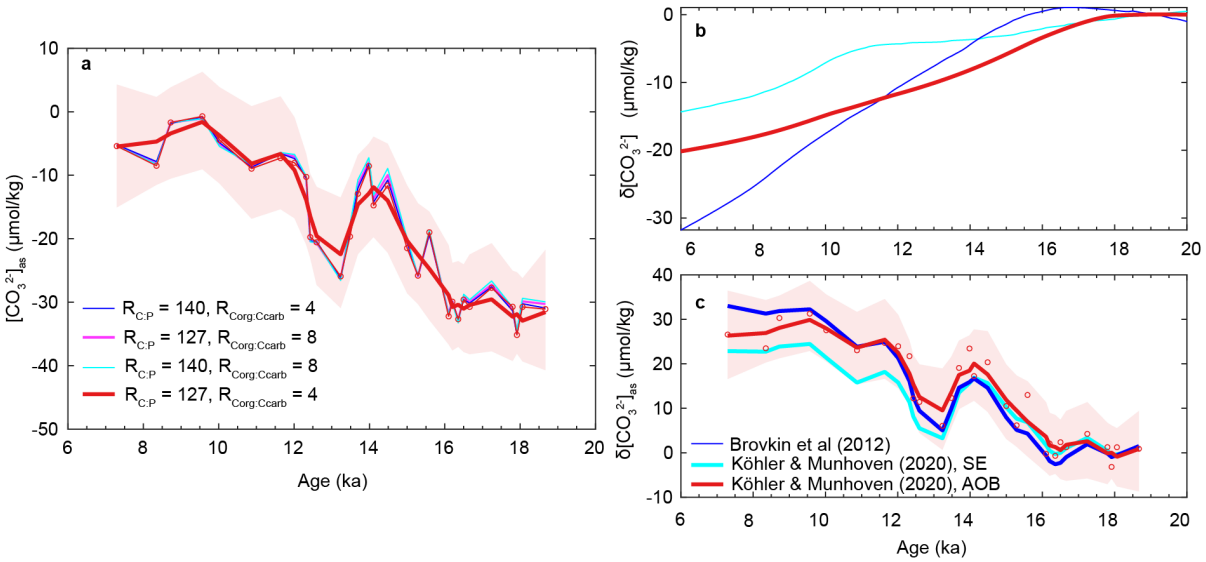

Supplementary Fig. 5. Sensitivity tests for deglacial $[CO_3^{2-}]_{as}$ at site MD97-2106. a, $[CO_3^{2-}]_{as}$ calculated using various sensitivities to evaluate effects from changes in organic matter composition ($R_{C:P}$) and rain ratio ($R_{Corg:Ccarb}$)[10]. Red curve with envelope is calculated using $R_{C:P}$ = 127 and $R_{Corg:Ccarb}$= 4 shown in the main text. **b,** Effects of the global alkalinity change on deep Southern Ocean $[CO_3^{2-}]$, assuming no air-sea CO_2 exchange from three different simulations[11,12]. **c**, changes in $[CO_3^{2-}]_{as}$ relative to the LGM calculated using three global alkalinity histories[11,12].

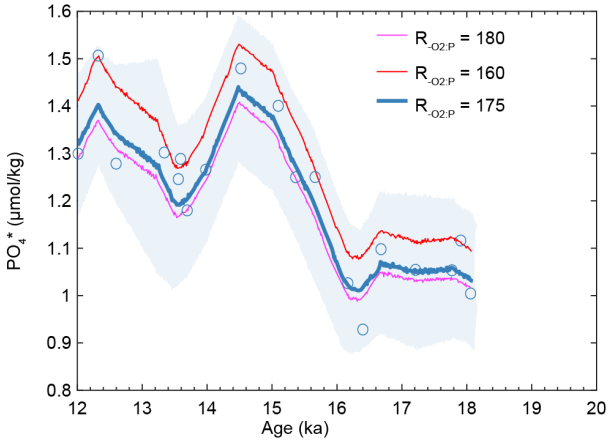

Supplementary Fig. 6. Deglacial PO_4* derived from different Redfield ratios ($R_{-O2:P}$) at site MD97-2106. The blue curve with circles and error envelope is based on a $R_{-O2:P}$ of 175 following the definition in Ref. [13,14]. Red and magenta curves are calculated using $R_{-O2:P}$ of 160 and 180, respectively, which encompasses the entire deep-water $R_{-O2:P}$ variability in the modern oceans[15].

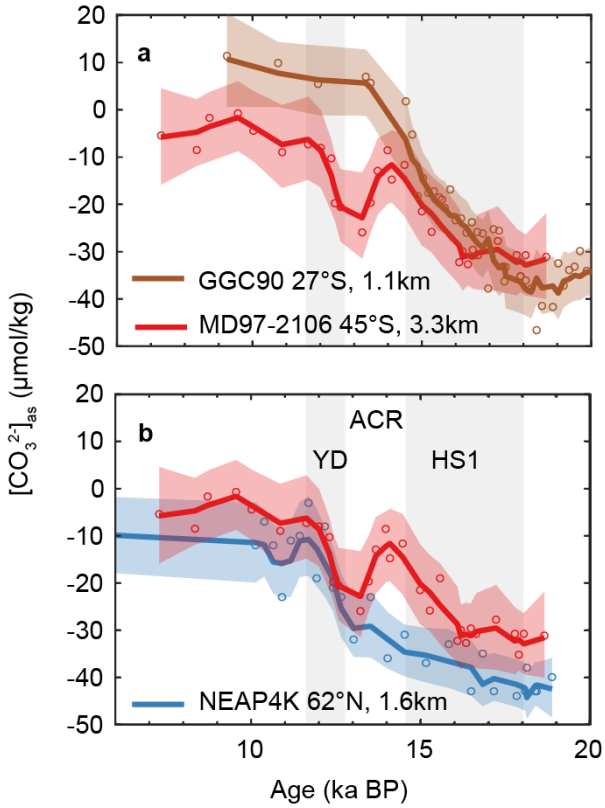

Supplementary Fig. 7. Comparisons of MD97-2106 $[CO_3^{2-}]_{as}$ with published records[16]. a, Results at MD97-2106 (this study) compared with those at core GGC90 (South Atlantic) bathed in the downstream of AAIW[16]. **b,** Results at core NEAP 4K bathed in the North Atlantic Deep Water[16] and at MD97-2106 (this study).

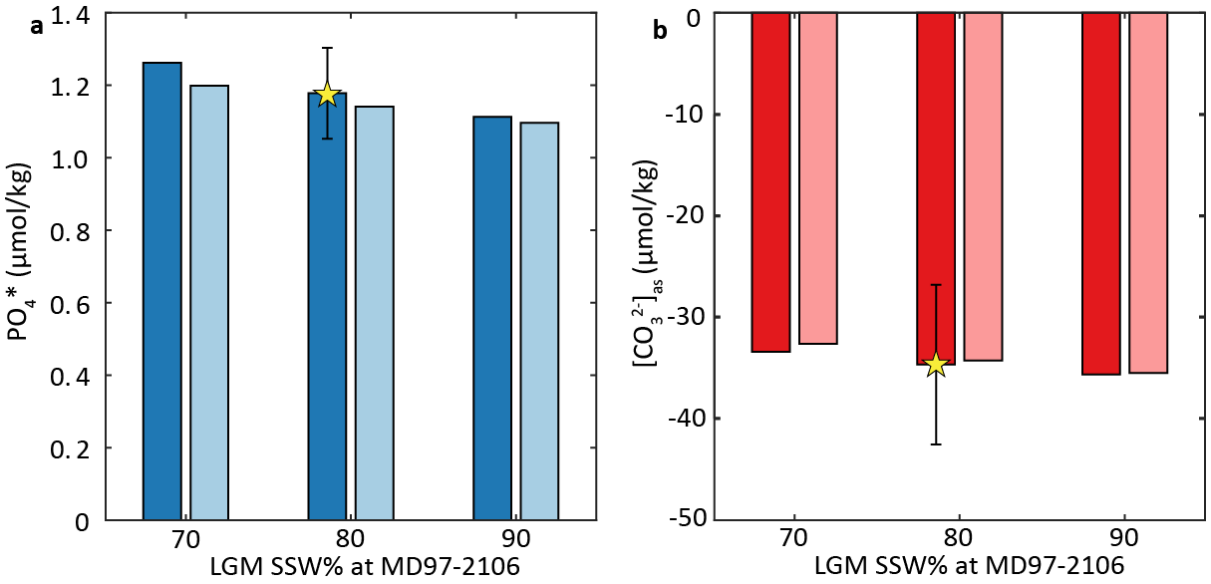

Supplementary Fig. 8. Sensitivity tests for LGM SSW PO_4* (a) and $[CO_3^{2-}]_{as}$ (b). LGM SSW PO_4* and $[CO_3^{2-}]_{as}$ are calculated based on varying SSW% (70%-90%) at site MD97-2106. In **a**, bars in dark and light blue, respectively, show LGM SSW PO_4* calculated assuming 20% decline and no decline in the NSW PO_4* during the LGM compared to the late Holocene. In **b**, bars in dark and light red, respectively, show LGM SSW $[CO_3^{2-}]_{as}$ calculated assuming 0% and 10% SSW at the NSW-dominated site NEAK-4K during the LGM compared to the late Holocene. Yellow stars highlight the preferred calculation discussed in the main text. Error bars show the ±1σ uncertainties associated with the reconstruction of the LGM SSW endmember values. These sensitivity tests show that LGM SSW PO_4* and $[CO_3^{2-}]_{as}$ calculated here are insensitive to LGM SSW% at site MD97-2106 and NSW endmember values.

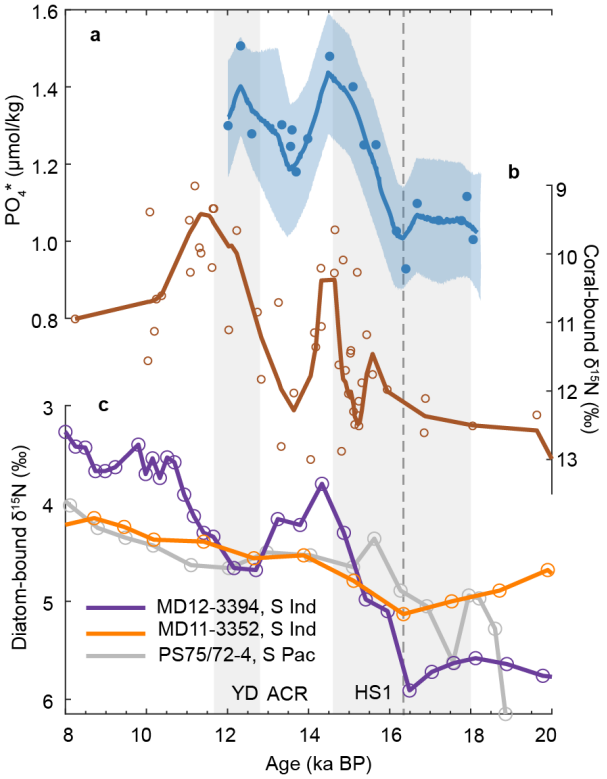

Supplementary Fig. 9. Comparison of deep-water PO_4* at MD97-2106 with fossil-bound $\delta^{15}N$ records from the Southern Ocean. a, Deep-water PO_4* at site MD97-2106. **b,** Coral-bound $\delta^{15}N$ from the Drake Passage[17,18]. **c,** Diatom-bound $\delta^{15}N$ from core located near the modern Antarctic Polar Front[19,20]. Despite weaker age constraints than coral-bound $\delta^{15}N$ records, diatom-bound $\delta^{15}N$ data show little change during early HS1 as revealed by the coral-bound $\delta^{15}N$ data. $\delta^{15}N$ data suggest reduced nutrient utilization and thus a weaker biological pump in the PAZ during late HS1, consistent with PO_4* at site MD97-2106.

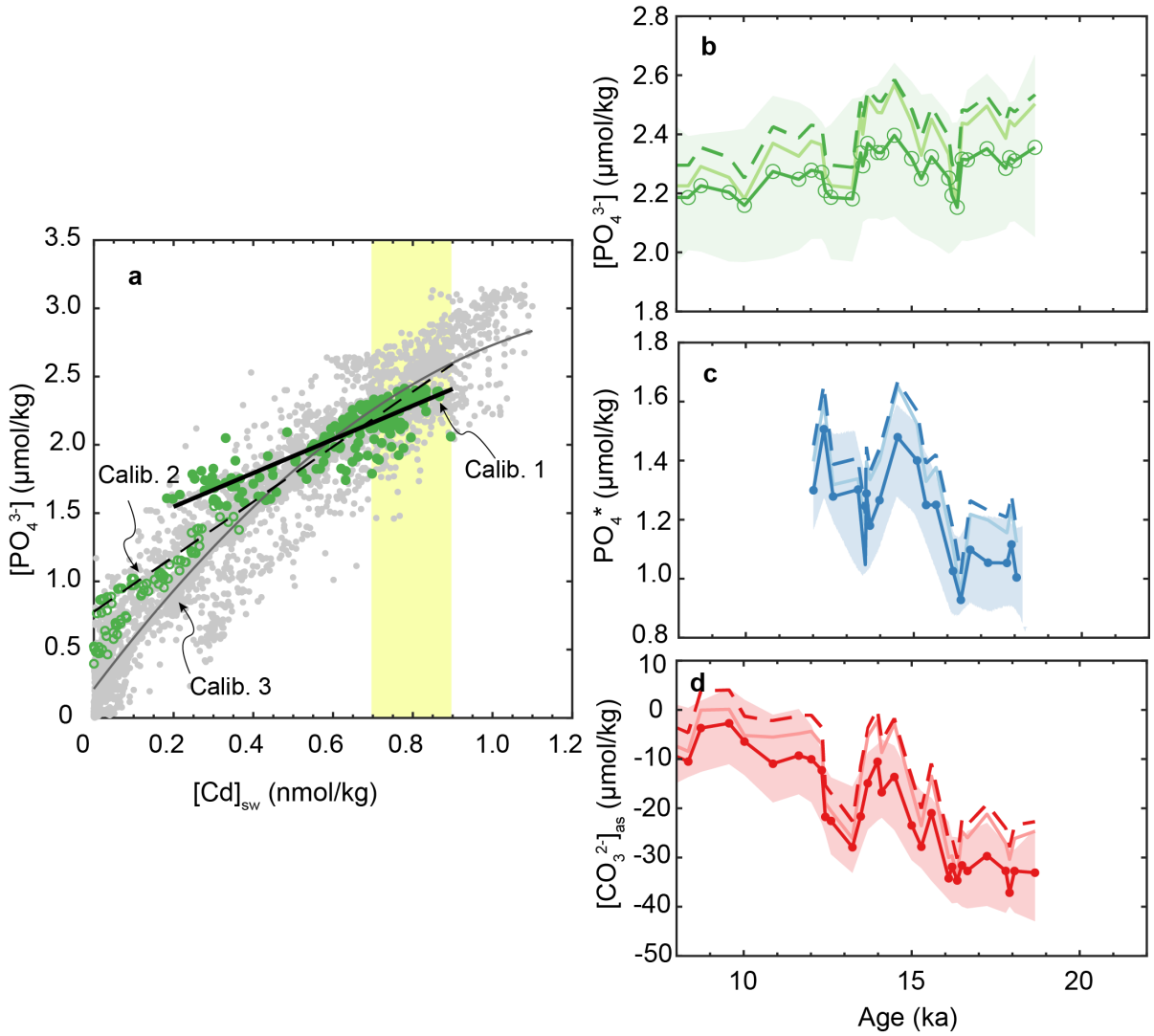

Supplementary Fig. 10. Sensitivity test of $[Cd]_{sw}$-$[PO_4^{3-}]$ calibrations on our reconstructions. **a**, modern seawater $[Cd]_{sw}$ and $[PO_4^{3-}]$ data from the GEOTRACES dataset[21]. Empty green dots are from GIPY06 Section south of Tasmania and filled green dots are sites with $[PO_4^{3-}]$ >1.5 µmol/kg. Calibrations 1 and 2 are linear calibrations based on GIPY06 data with $[PO_4^{3-}]$ >1.5 µmol/kg and all GIPY06 data, respectively. Calibrations 3 is quadratic calibration based on all GEOTRACES data. The yellow vertical bar highlights the $[Cd]_{sw}$ range reconstructed at site MD97-2106. **b**, Reconstructed $[PO_4^{3-}]$; **c**, PO_4*; and **d,** $[CO_3^{2-}]_{as}$. In **b-d**, bold lines with dots and shadings are reconstructions based on calibration 1 shown in the main text, while light-coloured lines and dashed lines are reconstructions based on calibrations 3 and 2, respectively. Different calibrations yield similar patterns of $[PO_4^{3-}]$, PO_4*, and $[CO_3^{2-}]_{as}$, despite their varying absolute values.

Supplementary references

1 Lauvset, S. K. *et al.* A new global interior ocean mapped climatology: the 1° × 1° GLODAP version 2. *Earth System Science Data* **8**, 325-340 (2016). https://doi.org:10.5194/essd-8-325-2016

2 Olsen, A. *et al.* GLODAPv2.2019 – an update of GLODAPv2. *Earth System Science Data* **11**, 1437-1461 (2019). https://doi.org:10.5194/essd-11-1437-2019

3 Rae, J. W. B. & Broecker, W. What fraction of the Pacific and Indian oceans' deep water is formed in the Southern Ocean? *Biogeosciences* **15**, 3779-3794 (2018). https://doi.org:10.5194/bg-15-3779-2018

4 Dai, Y., Yu, J. & Rafter, P. Deglacial Ventilation Changes in the Deep Southwest Pacific. *Paleoceanography and Paleoclimatology* **36** (2021). https://doi.org:10.1029/2020pa004172

5 Moy, A., Howard, W. & Gagan, K. Late Quaternary palaeoceanography of the Circumpolar Deep Water from the South Tasman Rise. *J. Quat. Sci.* **21**, 763-777 (2006). https://doi.org:10.1002/jqs

6 members, E. c. Eight glacial cycles from an Antarctic ice core. *Nature* **429**, 623-628 (2004). https://doi.org:10.1038/nature02599

7 Dai, Y., Yu, J., Ren, H. & Ji, X. Deglacial Subantarctic CO2 outgassing driven by a weakened solubility pump. *Nature Communications* **13** (2022). https://doi.org:10.1038/s41467-022-32895-9

8 Jaccard, S. L., Galbraith, E. D., Martinez-Garcia, A. & Anderson, R. F. Covariation of deep Southern Ocean oxygenation and atmospheric CO through the last ice age. *Nature* (2016). https://doi.org:10.1038/nature16514

9 Gottschalk, J. *et al.* Glacial heterogeneity in Southern Ocean carbon storage abated by fast South Indian deglacial carbon release. *Nat Commun* **11**, 6192 (2020). https://doi.org:10.1038/s41467-020-20034-1

10 Yu, J. *et al.* More efficient North Atlantic carbon pump during the Last Glacial Maximum. *Nat Commun* **10**, 2170 (2019). https://doi.org:10.1038/s41467-019-10028-z

11 Brovkin, V., Ganopolski, A., Archer, D. & Munhoven, G. Glacial CO₂ cycle as a succession of key physical and biogeochemical processes. *Climate of the Past* **8**, 251-264 (2012). https://doi.org:10.5194/cp-8-251-2012

12 Köhler, P. & Munhoven, G. Late Pleistocene Carbon Cycle Revisited by Considering Solid Earth Processes. *Paleoceanography and Paleoclimatology* **35** (2020). https://doi.org:10.1029/2020pa004020

13 Broecker, W. S. *et al.* How much deep water is formed in the Southern Ocean? *Journal of Geophysical Research: Oceans* **103**, 15833-15843 (1998). https://doi.org:10.1029/98jc00248

14 Broecker, W. S., Takahashi, T. & Takahashi, T. Sources and flow patterns of deep-ocean waters as deduced from potential temperature, salinity, and initial phosphate concentration. *J. Geophys. Res.* **90**, 6925 (1985). https://doi.org:10.1029/JC090iC04p06925

15 Anderson, L. A. & Sarmiento, J. L. Redfield ratios of remineralization determined by nutrient data analysis. *Global Biogeochem. Cycles* **8**, 65-80 (1994).

16 Yu, J. *et al.* Millennial and centennial CO2 release from the Southern Ocean during the last deglaciation. *Nat. Geosci.* (2022). https://doi.org:10.1038/s41561-022-00910-9

17 Li, T. *et al.* Rapid shifts in circulation and biogeochemistry of the Southern Ocean during deglacial carbon cycle events. *Sci Adv* **6** (2020). https://doi.org:10.1126/sciadv.abb3807

18 Wang, X. T. *et al.* Deep-sea coral evidence for lower Southern Ocean surface nitrate concentrations during the last ice age. *Proc Natl Acad Sci U S A* (2017). https://doi.org:10.1073/pnas.1615718114

19 Ai, X. E. *et al.* Southern Ocean upwelling, Earth's obliquity, and glacial-interglacial atmospheric CO2 change. *Science* **370**, 1348-1352 (2020). https://doi.org:10.1126/science.abd2115

20 Studer, A. S. *et al.* Antarctic Zone nutrient conditions during the last two glacial cycles. *Paleoceanography* **30**, 845-862 (2015). https://doi.org:10.1002/2014pa002745

21 Group, G. I. D. P. (ed NERC EDS British Oceanographic Data Centre NOC) (2023).